Direct Imaging and Location of Pb^{2+} and K^{+} in EMT Framework Type Zeolite

Yaping Zhang, Daniel Smith, Jennifer E. Readman* and Alvaro Mayoral *

Instituto de Nanociencia y Materiales de Aragón (INMA), CSIC-Universidad de Zaragoza, Zaragoza 50009.

ABSTRACT: The understanding of the structural framework and metal locations within zeolites are two critical aspects in order to tune and further exploit their properties as heterogeneous catalysts, advanced optical devices or as water remediation materials. The development of electron microscopy has made it possible to observe directly, the zeolitic framework and the distribution of extra-framework cations within the pores at the atomic level. Here, we have studied the **EMT** framework providing data with unprecedented spatial resolution, which have allowed the analysis of the **FAU** domains present in the framework. Additionally, the potassium and lead, (introduced by aqueous ion exchange) which were non-periodically distributed in the pores have been located. An alternative image mode, annular bright field (ABF), has been used proving its usefulness to extend the spatial resolution and increase the sensitivity towards light elements such as bridging oxygen. Finally, the combination of atomic imaging (local information) with the three- dimension electron diffraction tomography (3D-EDT) analysis (averaged information) allowed determining the Lead-**EMT** crystal symmetry to be $P6_3mc$.

1. INTRODUCTION

Zeolites are microporous materials with tunable porosity widely used as ion exchangers or heterogeneous catalysts[1] among many others applications. They are able to confine elements within their pores and they also exhibit very good thermal stability[2-4]. Due to the confinement capability that zeolites exhibit, they can protect extra-framework species, minimizing their agglomeration and release back to the environment as well as tuning their physical properties (work function or luminescence for example) [5-18].

There are currently up to 253 different zeolite topologies[19] in the International Zeolite Association (IZA) structure database; among them, **TSC**, **EMT** and **FAU** exhibit the lowest framework densities of 13.2~13.3 T/1000 Å^3. Lower density zeolites are highly desirable for soil treatment applications[20] or catalysis[21]. **EMT** was firstly synthesized in 1971[22] as a mixture between **FAU** and **EMT**. The pure **EMT** framework, named EMC-2 after **E**lf (or Ecole Supérieure) **M**ulhouse **C**himie - two, was obtained by Delprato and co-workers[23] in 1990 and the structure was completely solved by Baerlocher *et al*. four years later[24]. **EMT** is the hexagonal polytype of the **FAU**-type zeolite (cubic) sharing the same layer units composed of *sodalite* cages (*t-toc*) linked by double 6-membered rings (d6R, *thpr*). The **EMT** framework contains large *t-wof* and *t-wou* cages with three and five 12-membered ring (12MR) windows respectively. In contrast with the zigzag channels of **FAU** and the 8-membered ring windows of **TSC**, **EMT** has straight access along three directions, all with 12MR windows. **EMT** has previously been used in biomedicine[25] and gas capture and separation[26]. It also shows great potential for industrial applications such as petroleum cracking due to its large channel and cavity size.

Besides the use of zeolites as heterogeneous catalysts and water softeners, the capability of zeolites to capture different elements within their pore system is also attractive for various applications such optoelectronics or water remediation. The interest of occluding lead within the pores of zeolites or metal organic frameworks (MOFs) has re-gained much interest due to the possibility of tuning the optical response of lead-loaded zeolites while preventing lead discharge into the environment due to its coordination to the framework. The incorporation of lead species can be summarized in three families: (i) Unitary: Clusters (including single atom) with only one element[14, 27]; (ii) Binary: Species formed by two elements, such as PbS, PbI_2, located inside the zeolite frameworks[28-31]; (iii) Ternary: Lead compounds formed by three elements, $CsPbI_3$ and $CsPbBr_3$[32].

To gain structural information, there are several characterization methods available to help explain the physicochemical properties of zeolites. Such properties are strongly affected by the type of metal introduced, its size and location; therefore, characterization at atomic level is becoming indispensable to tailor the properties of materials at the nanoscale. Zeolite frameworks present high degree of symmetry, whereas the exchanged forms are usually disordered. Therefore, long-range techniques such as X-ray diffraction and Rietveld analysis do not always give the short-range information needed. In this sense, transmission electron microscopy is perhaps, the most powerful methodology as it can provide direct visualization

of the framework and the guest species at an atomic level together with crystallographic and chemical information[33-37]. All these results have been achieved with thorough control of the electron dose, as zeolites are strongly beam sensitive. Working in probe mode offers a quick scan, reducing the sample damage. The possibility of obtaining sub-Ängstrom probes together with the use of several detectors simultaneously allows for the collection of signals at high angle (annular dark field, ADF) providing information regarding the heavy elements. Meanwhile, an angular bright field detector (ABF) enhances the signal of light compounds[38-39], which are scattered at low angle. Therefore, by combining the information from both detectors, determining the location and element type of both light and heavy elements is achievable.

In this work, **EMT** framework type zeolite was ion exchanged with $Pb(NO_3)_2$ to finally obtain a partially loaded Pb-**EMT**. The characterization has been primarily carried out by Atomic-resolution transmission electron microscopy imaging that has been acquired by combining ADF and ABF detectors to obtain atomically resolved data of the framework and on the extraframework cations. These observations have been correlated with the data obtained by electron diffraction tomography. The existence of **FAU** intergrowths have been also analyzed based on this technique.

2. METHODS

2.1 Synthetic procedures. Pb-EMT: **EMT** was synthesized using previously reported method[23, 40]. 1.45 g of sodium aluminate and 1.21 g of 50% NaOH solution was added to 7.8 g of deionized water, together with 1.76 g of 18-crown-6 and stirred vigorously. Once homogeneous 15.4 g silica solution (LUDOX AM-30) was added with stirring and left for 24 days at room temperature to incubate. The mixture was placed in a 45 mL Parr pressure vessel and heated for 12 days at 110°C. The product was filtered and washed with copious amounts of deionized water, then calcined in air at 540°C for 16 hours.

A potassium ion-exchange was performed by adding 4 g of EMT to 500 mL of 0.1 M KNO_3 solution and stirred overnight. The powder was recovered and washed with 1 L of distilled water and air-dried overnight. The exchange procedure was repeated a further two times.

The lead ion-exchange was carried out as follows, 2 g of EMT was added to 500 mL of 0.1 M $Pb(NO_3)_2$ solution and stirred overnight. The powder was recovered and washed with 1 L of distilled water and air-dried overnight. The exchange and washing procedures were repeated a further two times.

2.2 Characterization. Scanning Electron Microscopy: STEM STEM analyses were carried out in a JEOL Grand ARM 300, equipped with a cold Field Emission Gun (cold FEG) and operated at 300 kV. The column was fitted with a JEOL double aberration corrector, which was aligned prior the analyses to assure a maximum spatial resolution of 0.7 Å in scanning mode. The microscope was also equipped with a JEOL EDS and a Gatan Quantum Energy Filter for spectroscopic measurements.

3D-EDT: The 3D-EDT data was collected using JEOL.Shell software in a JEOL JEM2100 Plus electron microscope operated at 200 kV in transmission electron microscope (TEM) mode. A total collecting angle of 120 degrees was obtained by tilting the sample holder from -60° to +60°. The intensities were extracted with EDT.Process software. Finally, the structure was solved with Sir2014[41].

Energy Dispersive X-ray Spectroscopy (EDS): EDS data was collected using a JEOL JEM2100 Plus operated in STEM mode with an accelerating voltage of 200 kV.

Scanning Electron Microscopy (SEM): The Scanning Electron Microscope (SEM) images were collected in a JEOL JEM7800 Prime with a work distance of 7 mm under a landing voltage of 1 kV.

STEM simulation: The simulated ADF-STEM and ABFSTEM images along [100] were obtained with software QSTEM[42]. A supercell of **150 × 150 × 150** Å^3 was constructed for a pure silica EMT. The probe array was **600 × 600 pixels** with 0.032 Å resolution with the slice thickness of 1 Å. The detector geometries inner and outer angles were 50-200 mrad for ADF and 5-40 mrad for ABF.

Image treatment: In order to minimize the beam damage, the electron dose was significantly reduced in comparison with standard STEM conditions. For the current experiments, the total time for image acquisition ranged from 6 to 10 seconds, 1024 × 1024 pixels using an electron dose of 1120 $e^-/Å^2$ to 2800 $e^-/Å^2$. Under these conditions, images could be directly interpretated and all intensity analyses were performed over raw data. However, for a clearer visualization of the frameworks and of the light cations Random Noise 2D difference filter was used[43] from HREM Research Inc.

3. RESULTS & DISCUSSION

The **EMT** framework type is a zeolite with hexagonal symmetry and $P6_3/mmc$ space group. The lattice constants previously reported are $a = b = 17.215$ Å, $c = 28.082$ Å, $\alpha = \beta = 90°$ and $\gamma = 120°$. The morphology of the **EMT** particles was in agreement with the hexagonal symmetry presenting well-defined hexagonal particles with a thickness up to 500 nm and widths that reached up to several microns, see Figure 1.

This framework is formed by double six rings (d6Rs) and *sodalite* (*sod*) cages that when connected, forming *faujasite* layers (layer unit), with 12-membered rings formed along the *b* and *c* directions. The stacking sequence of these layers allow the formation of either **EMT** or **FAU**. By AA' stacking of *faujasite* sheets, **EMT** is obtained, where the adjacent two layers are related to each other through a mirror plane. Alternatively, in **FAU**, the stacking sequence is ABC, with each *faujasite* layer rotated 60° with respect to the previous one, and each *sod* cage related to its partner by an inversion centre.

For **EMT**, along the *b* axis, the 12MRs run parallel to the observation axis while the layer unit run perpendicular

along the c axis in an AA'A stacking. The chemical formula for calcined EMC-2 has been reported to be $[Na_{20}(H_2O)_6][Si_{76}Al_{20}O_{192}]$-**EMT**, where the 20 Na^+ cations that compensate the presence of Al tetrahedra, sit in three crystallographic sites at X2: 0.5890, 0.1770, 0.0470; X3: 0.6667, 0.3333, 0.6270; X4: 0.3571, 0.1790, 0.3880 with 0.25, 0.32 and 0.33 site occupancy respectively, see Figure S1. In Figure S1, the T (T=Si and Al) atoms are presented as blue, brown, purple and green spheres corresponding to the different crystallographic sites, O in red, while X2 appears in yellow, X3 light blue and X4 in pink being all of them associate to the 6SRs of the *sod* cages.

Analysis of FAU intergrowths. It has been previously mentioned that due to the structural similarities, (the use of the same building units differing only on how the layers stack) **FAU** and **EMT** can coexist in the same crystals[23, 37, 44]. Along [110] orientation, both hexagonal **EMT** and cubic **FAU** exhibit different manners of pillaring the *faujasite* layers; while for **EMT** there is a AA´AA´... stacking (Figure 2a) for **FAU** (Figure 2b) it follows ABC.. pillaring. These layers are formed by *sodalite* cages (*t-toc*), in pink, linked by d6Rs (*t-hpr*), purple, which are subsequently connected by also d6Rs (*t-hpr*) shown in green between different layers. An isolated *faujasite* layer is depicted in Figure 2c.

Because of these structural similarities, it could be expected that intergrowths of both phases due to the layer stacking sequence in a defective way would exist. In fact, there are many cases where **EMT** has been crystallized with the presence of **FAU**[45-47]. For **EMT** A and A´ layers are mirror related to each other[48]. While in **FAU**, layer B is shifted (1/2*a*, 1/2*b*, 1/2*c*) relative to layer A and layer C is shifted (1/2*a*, 0, 1/2*c*) relative to layer A. The origin of the A, B, C layers are marked in the Figure 2d. Large *t-wou* and *t-wof* cages for **EMT** and *t-fau* cages for **FAU** are formed between layers. *t-wof, t-wou* and *t-fau* have 3, 5 and 4 12MRs windows respectively.

Figure 2e corresponds to the C_s-corrected STEM ADF image of an **EMT** crystal with structural defects in the framework evidenced by the diffuse spots (yellow arrows) in the Fourier diffractogram, Figure 2e inset. This region, of approximately 6 nm along $[110]/[100]_{EMT}$ zone axis, corresponds to a **FAU** domain, enclosed by **EMT** regions. In another crystal, the sequence AA'ABB'A'AA' can be observed, Figure 2f. This region is formed by two **FAU** domains connected through a mirror plane (defined by BB' layers) enclosed within the **EMT**. For direct interpretation, the schematic model has been superimposed displayed in different colors to distinguish the three zones as shown in Figure 2f. The left (green) and right (yellow/red) regions, corresponding to the **EMT** framework, allow the clear visualization of the 12 MRs, marked by blue dashed circles. While in between, the twin plane is marked in pink color. By observing this structure along the [001] projection, Figure 2g, these two **EMT** domains would overlap, where the 12 MRs marked with a blue background, would be blocked by *sodalite* cages from the twin plane, BB', shown in Figure 2f. The large 12MR windows of the BB' stacking would be also blocked by the **EMT** sodalite cages from both sides as shown in Figure 2g. By observing figure 2f, yellow circles, it can be appreciated the existence of a faint signal inside the 12MRs in the twin plane that is associated with the presence of *sodalite* cages from the **EMT** region, partially blocking these channels. These 12MRs are fully empty in the **EMT** area (blue dashed circles).

Analysis of EMT framework and extraframework cations. It is possible to synthesize the **EMT** framework with different Si/Al ratios, but in general terms, the most common zeolite obtained has been EMC-2 with a chemical formula $|Na_{20}(H_2O)_6|\ [Si_{76}Al_{20}O_{192}]$[23-24]. In this work, Energy-dispersive X-ray spectroscopy (EDS) analyses were used to estimate the chemical composition of the current **EMT**. The results obtained were reasonable and in agreement with the data reported. The most relevant differences with previous works were that K^+ was also used as counter ion together with Na^+, and that Pb^{2+} was also detected due to the ion-exchange. The averaged results after analyzing 12 different crystallites, table S1, were $|(Na_4+K_{10})Pb_2|\ [Si_{76}Al_{20}O_{205}]$. Based on these results, the electro-neutrality would be maintained as the sum of the positive charges from the cationic species would be 18 that would compensate the 20 (AlO_4^-) of the framework. The small mismatch between the cations and aluminum is related to a slight experimental error of the technique or to the presence of protonic species H^+ from the water. In fact, the excess of O detected could be associated to water adsorbed in the pores. For simplicity, hereafter, we will refer only K^+ when considering both Na^+ and K^+ as due to their low content and similar atomic number it is not possible to distinguish between both metals.

Annular Dark Field (ADF) together with Annular Bright Field (ABF) imaging modes can reveal unique information especially at local level. By using an ADF detector, the electrons scattered at high angle are used to form the images allowing the visualization of heavier elements as the signal is proportional to $Z^{1.6\sim2}$[49-50], where Z is the atomic number. On the other hand, ABF provides complementary information of the framework, as it is more sensitive to light compounds, even with higher spatial resolution [36, 38-39].

For the **EMT** framework type, the most suitable projections for the structural observation are [110]/[100] two equivalent orientations with the minimum atomic column overlapping; hereafter, we will refer only to [100] for simplicity. Figure 3a corresponds to the C_s-corrected STEMABF micrograph of Pb loaded **EMT** zeolite along [100] orientation; in this case, the atomic columns appear as black dots and the big pores which are clearly observable correspond to the 12MRs. The white arrows point to a structural defect resulting for the merge of two *faujasite* sheets which breaks the AA'A stacking, the FD, shown inset, proves that the spatial resolution that can be achieved is at least 1.2 Å represented by the 00024 diffraction spot, marked by a yellow circle. The symmetry-averaged image is depicted in figure 3b; although the ABF data already presents sufficient degree of quality to analyze the structure at atomic level, the averaged data is displayed to facilitate the observation of some particular aspects. Symmetry

averaging image treatment presents certain advantages as it allows discussion about plane symmetry elements and it significantly increases the signal-to-noise ratio. On the other hand, it introduces undesired periodicity, which is disadvantageous for non-periodic materials such as zeolites with uneven cationic distribution. Here, symmetry averaging has been used to improve the signal-to-noise ratio; for **EMT** topology the reported space group is $P6_3/mmc$ (194); therefore, its plane group along the [100] should be *pmg*. The averaged data assuming this space group is depicted in figure 3b highlighting i) T atoms (blue arrow); ii) Oxygen bridges (red arrows) and additional signals that are not part of the framework (pink and yellow arrows). To facilitate the interpretation, the model of the framework has been superimposed where the Si appears in blue and O in red, for clarity, the presence of extraframework cationic species has been omitted. Figure S2 compares the experimental data (Figure S2a) with the simulated image (Figure S2b) of the all-silica framework (without cationic species to highlight the differences between the bare framework and the experimental data) Figure S2b; in both cases, colored arrows have been used to point the framework atoms and the extraframework sites. Figure 3b exhibits excellent image quality and it corroborates the feasibility of ABF imaging for the observation of light compounds as oxygen bridges. In addition, the two distinct signals that do not belong to the framework can be inferred to be cationic species; however, an aspect that need to be considered is that, to obtain this image, symmetry restrains have been introduced and the presence of those extraframework species do not necessarily need to be periodic. In order to evaluate this aspect and to study the possible introduction of Pb^{2+} in the pores after ion exchange, we turned into C_s-corrected STEMADF without imposing any symmetry averaging, Figure 4.

Figure 4a depicts the correspondent C_s-corrected STEMADF data of the Pb-**EMT** zeolite on the [100] projection, in here, the contrast is reversed respect to the ABF data where the atomic columns appearing as bright spots and in which the 12 MRs are observed together with the d6Rs and the *sodalite* cages. Interestingly, a strong contrast is observed as bright spots, which appear at specific sites in a non-periodic manner. The areas marked by rectangles with different colors, numbered 1 to 3, were enlarged to analyze the contrast variations at different regions of the crystal, while the additional dashed yellow rectangle corresponds to the area that is magnified in Figure 4b. The intensity profiles along several *sodalite* cages were extracted (Figure S3) observing some maxima corresponding to those bright spots. In Figure 4a, the 12 MRs are clearly visualized as empty pores; meanwhile the bright spots would be placed at those sites where Na^+ have been proposed to occupy, corresponding to the X3 and X4 sites. This observation is in agreement with the data obtained with an ABF detector (see Figure 3b yellow arrow) that indicates a very strong signal (that appears periodically due to the symmetry averaged introduced) near the oxygen bridges. Such signal observed in the ABF and in the ADF cannot derive from the O bridges, due to their low scattering factor, and therefore it is owed to the presence of single Pb^{2+} sites, single atoms or atomic columns. Due to the low initial occupancy of the extraframework cations (K^+ and Na^+ here), it cannot be estimated whether Pb^{2+} is in the form of single atoms or if there are several Pb^{2+} on the same column. Nevertheless, X3 and X4 sites correspond to two distinct atomic sites with different coordinates; however, due to their proximity in the projected image ≈ 0.5 Å it cannot be initially distinguished whether Pb^{2+} replaced X3, X4 or both.

To deeply investigate the ion-exchange capability and therefore the location of the cations, Figure S4a shows the schematic model of a *sodalite* cage with the same color code as Figure S1 a color code that displays T3 (T=Si, Al) crystallographic sites in purple, forming an s6R, where the light blue sphere corresponds to the cationic site at X3. Blue T atoms correspond to T1; brown spheres are the T2 sites, purple T3 and in green ones the T4. Cations at X4 are marked in pink, while cationic sites at X2 appears in yellow. If Pb^{2+} would occupy X4 site, this would correspond to the location of Pb^{2+} on top of the S6Rs of the *t-toc* cage, see figure S4a. On the other hand, if Pb^{2+} would replace X3 this one would be in a similar position, on top of another S6Rs of the *t-toc* cage, but closer to the framework. Figure S4b presents an entire unit cell with the same color code showing, along this projection, the proximity between X3 and X4. It is important to mention that no experimental evidence was found of Pb^{2+} occupying the X2 sites, that in the projected image would be inside the s6Rs very close to T1 atoms.

The other extraframework signal that was detected in the experimental data that did not belong to the zeolitic framework was observed within the s6Rs but not as intense as the aforementioned one associated to Pb^{2+}. In this case, the signal marked by a pink arrow in the ABF data, figure 3b, and by a pink dashed circle in figure 4b, would correspond to K^+ cations (based on the chemical analyses the K^+ content is much higher in comparison with Na^+, although because of their similar atomic number it would not be possible to distinguish between them). These extraframework species were not periodically distributed along the entire framework, as empty s6Rs could also be identified, see dashed blue circles in Figure 4b. This observation could be associated to the presence of aluminum in the framework suggesting that the aluminum was not periodically distributed as the empty s6Rs would be linked to the absence of Al at those sites; meanwhile the extraframework cationic presence suggest the existence of Al around them. Figure 4c depicts an enlarged image of a 12 MR, obtained from the yellow dashed rectangle in figure 4b, where the K^+ can be identified within the s6R. Two different intensity profiles were plotted along the arrows 1 and 2, figure 4d, where two peaks are present, the first one and more intense, corresponds to an atomic column of the framework, Si or Si+Al; while the other belongs to the K^+. The measured projected distances were d1 = 2.05 Å

corresponding to the distance between T2-cation and d2 = 2.28 Å corresponding to the distance between the T4-cation, these measurements (slightly shorter) are in agreement with the data reported for Na-**EMT** (for X4 sites), where projected distances are 2.20 Å and 2.42 Å, respectively. Furthermore, no evidences of K^+ or Pb^{2+} present at X2 sites were found in any of the equivalent sites.

Based on these observations, Pb^{2+} would preferentially replace the cations at the X3 sites, figure 4b yellow arrows. Despite that X3 and X4 sites are too close to be distinguished, we have not observed evidences of the presence of Pb^{2+} at the s6Rs denoted by pink dashed circles in figure 4b; that would correspond to K^+ at X4 sites. Therefore, as the K^+ at X4 sites have two equivalent positions if Pb^{2+} would enter at X4; this stronger signal would be observed at the sites indicated by a pink circle and at the sites pointed by yellow arrows. As this is not the case, it is possible to conclude that Pb^{2+} would only go into the sites denoted as X3; in fact, as K^+ is at X4 the total signal detected at X3 would be mostly owed to Pb^{2+} but with a contribution from K^+ situated at X4. Despite that, the Pb^{2+} signal was not homogeneously observed along the entire crystal, it always occupied a particular crystallographic site; however, due to the low occupancy of the extraframework cations, 0.33 for X4, it does not appear along the entire crystal. From these observations, it can be also inferred that Pb^{2+} would compensate the electric charge of the cations at X2 sites; as from the experimental data no signal was detected at these positions suggesting that the cations were removed from these sites but Pb^{2+} did not fill the positions; the electroneutrality was maintained as one Pb^{2+} would compensate two monoatomic species of either Na^+ or K^+. For comparison, simulated data were compared with the experimental data, see Figure S5. Figure S5a corresponds to the simulated image of the **EMT** framework with no cations added to the structure, Figure S5b displays the same image with different amounts of K^+ and Pb^{2+} added to the system. The blue dashed circle corresponds to a s6R where the K^+ are not observed, the amount of K^+ which was placed at that site was 6 atoms in that column; therefore, for a given thickness of 8 nm (≈ 4 unit cells) 6 atoms of K^+ per column were not detectable. The pink dashed circle corresponds to the K^+ at the s6Rs (18 atoms per column, which are clearly visible). Meanwhile, the yellow arrow points at the signal owed to the Pb^{2+} (in this case the column was filled by 6 atoms). Figure S5c corresponds to the experimental data obtained.

Framework analysis and crystallographic determination of Pb^{2+}, K^+ position. It has been proved so far, how image analysis at the atomic level can provide local information of the zeolitic framework and extraframework cations. On the other hand, electron diffraction can deliver more general information as the solution obtained is based on an average over several unit cells. The structure of Pb**EMT** zeolite was solved based on the diffraction intensities extracted from the 3D-EDT using direct methods. Figure S6 displays the extracted electron diffraction patterns along the main crystallographic orientations Figures S6a, S6b and S6c belongs to the *c**, *b** and *a** projections respectively. Along *c** axis, this zeolite exhibits 6-fold symmetry, while two perpendicular mirror planes are present along the other orientations, running along *a**, *b** and *c** axes, see Figures S6b and S6c. From the *hhk* plane (Figure S6d) the reflection condition *00l: l=2n* was confirmed, marked by a blue rectangle. For *hk0, hk1, hk2, hk3* planes, *hhl* and *h-hl* (*l* = 1, 2, 3, 4) reflections are marked with green and pink rectangles respectively. Reflections *h-hl* appear in all the four layers while *hhl* only appear when *l* = 2*n* (Figures S6e-h). These reflection conditions are in agreement with the extinction symbol *P_ _ c*. Thus, only three space groups fulfill these conditions $P6_3mc$ (186), *P*-62*c* (190), $P6_3/mmc$ (194). The three of them were used to solve the structure obtaining reliable results when $P6_3mc$ and $P6_3/mmc$ were used. Therefore, the space group chosen for solving the framework was $P6_3/mmc$ (194) in agreement with the previously reported data[24]. The data extracted from 3D-EDT can be also be used to gain additional information of the extraframework cations (Pb^{2+} and K^+). The initial solution and the correspondent intensity histogram are shown in Figures 5a and 5b respectively. The signals denoted as X1 and X2 are extraframework atoms situated outside the sodalite cages. X1 sitting inside the *t-wof* cage has 4 equivalent sites, represented as green spheres; meanwhile, X2 situated within the large *t-wou* cages has 12 equivalent sites per cell, rose spheres. The fact that the X1 site is not part of the framework and that it presents higher intensity indicates that the signal may correspond to a heavier element. These results are in concordance with the experimental atomic resolution data presented in figures 3 and 4 along the [100] projection, corroborating that the Pb would occupy X1 site, yellow arrows in Figures 3 and 4. Although the averaged solution from 3D-EDT suggested four equivalent positions, the experimental C_s-corrected data revealed that that Pb did not occupy all the four sites; instead, Pb atoms situated opposite to each other corresponding to either Pb_A or Pb_B in Figure 5a. Based on these observations, not only considering the framework but also the presence of Pb, if two Pb atoms from either Pb_A or Pb_B sites are removed the space group would lower its symmetry changing from $P6_3/mmc$ to $P6_3mc$, see Figure 5c where the two Pb atoms (green spheres) are marked by yellow circles. On the other hand, the intensity of X2 was slightly lower than the framework oxygen and its location was also found in the extraframework, Figure 5b. This signal is associated to the s6Rs of the *t-wou* cages; thus, the lower intensity signal and the fact that it does belong to the framework it allowed us to deduce that such signal can be attributed to a light cation Na^+/K^+. Some of the X2's symmetric equivalent sites overlap the Pb along [110]/[100] projections as shown in Figure 5c, but they are in different cages.

By comparing the experimental data acquired by C_s-corrected imaging at atomic level it was possible to elucidate preferential sites for Pb^{2+} and for K^+ evaluating also the ion exchange capability and which sites are more suitable to be initially exchanged. The electron diffraction

data allowed the characterization over an averaged volume of the structure obtaining results, which were in agreement with the observations by C_s-corrected STEM, allowing us to conclude that Pb^{2+} locates in the *t-wof* cage and K^+ locates in the *t-wou* cage. The most significant difference between the images and the diffraction data was that images showed preferential sites for Pb^{2+} and K^+, and that by imagining it was possible to acquired local information observing the absence of cations at positions that based on the electron diffraction should be occupied. This is because the results obtained by electron diffraction were averaged over a relatively large area (100 nm, limited by the diffraction aperture used. Therefore, the atomic coordinates described as X1 and X2, which were not part of the zeolite framework were the result of no single atoms but the preferential sites for cationic occupancy that in average tend to go to those sites. Table S2 presents the atomic coordinates obtained. These results illustrate the importance of combining electron diffraction with atomic resolution imaging to achieve a complete characterization of the structure of zeolites especially with the intention of gaining information at local level.

4. CONCLUSIONS

In conclusion, a combination of various electron microscopy techniques has been used to analyze the structure and the ion exchange capability of **EMT** zeolite, where K^+ and Pb^{2+} were both introduced in the pores. By taking a multitechnique approach, the particular features of Pb-**EMT** have been revealed. SEM data allowed the morphology visualization obtaining symmetry elements, which facilitated the structural solution.

C_s-corrected STEM observations displayed data with enough quality to obtain atomic resolution information, even showing the oxygen bridges as well as cations Pb^{2+} and K^+ that were atomically distributed over the framework. The atomic coordinates were determined by 3DEDT. Both the Pb^{2+} and K^+ were found to be outside the *sodalite* cages above the s6Rs of these cages. While Pb^{2+} was in the *t-wof* cages K^+ was in *t-wou* cages. Overall, atomic resolution images provided insights of the local structure of Pb-**EMT** gaining information on the ion exchange capability and on the location and periodicity of the extraframework cations, which helped to achieve a more accurate structural solution. The combination of 3DEDT with the image analysis concluded that crystal symmetry had to be reduced from $P6_3/mmc$ to $P6_3mc$.

ASSOCIATED CONTENT

Supporting Information. "This material is available free of charge via the Internet at http://pubs.acs.org." Experimental details, including chemicals, synthesis and characterization techniques.

AUTHOR INFORMATION

Corresponding Authors

Alvaro Mayoral - *Instituto de Nanociencia y Materiales de Aragón (INMA), CSIC-Universidad de Zaragoza, Zaragoza 50009.*
Center for High-Resolution Electron Microscopy (ChEM), School of Physical Science and Technology (SPST), ShanghaiTech University, 393 Middle Huaxia Road, Pudong, Shanghai.
Advanced Microscopy Laboratory (LMA), University of Zaragoza, 50018 Zaragoza, Spain.; orcid: 0000-0002-5229-2717; Email: amayoral@unizar.es

Jennifer E. Readman - *School of Physical Sciences and Computing, University of Central Lancashire; orcid:* 0000-00028170-5533*; Email: JEReadman@uclan.ac.uk*

Authors

Yaping Zhang - *Center for High-Resolution Electron Microscopy (ChEM), School of Physical Science and Technology (SPST), ShanghaiTech University, 393 Middle Huaxia Road,*
Pudong, Shanghai; orcid: 0000-0001-7362-4381

Daniel Smith - *School of Physical Sciences and Computing, University of Central Lancashire, United Kingdom; orcid: ; Email: JEReadman@uclan.ac.uk*

Author Contributions

The manuscript was written through contributions of all authors. / All authors have given approval to the final version of the manuscript. /

ACKNOWLEDGMENT

We deeply thank Professor Osamu Terasaki for fruitful discussions. The authors would like to thank The Centre for Highresolution Electron Microscopy (*ChEM*), supported by SPST of ShanghaiTech University under contract No. EM02161943; to the National Natural Science Foundation of China NFSC21850410448 and NSFC- 21835002. AM also acknowledges to the Spanish Ministry of Science trough the Ramon y Cajal program (RYC2018-024561-I) and to the regional government of Aragon (Spain) (DGA E13_20R). This project has received funding from the European Union's Horizon 2020 research and innovation programme under grant agreement No 823717 – ESTEEM3.

REFERENCES

(1) Li, Y.; Li, L.; Yu, J., Applications of Zeolites in Sustainable Chemistry. *Chem.* **2017**, *3*, 928-949.

(2) Atienzar, P.; Valencia, S.; Corma, A.; Garcia, H., Titanium-Containing Zeolites and Microporous Molecular Sieves as Photovoltaic Solar Cells. *Chemphyschem.* **2007**, *8*, 1115-9.

(3) Koeppe, R.; Bossart, O.; Calzaferri, G.; Sariciftci, N., Advanced Photon-Harvesting Concepts for Low-Energy Gap Organic Solar Cells. *Sol. Energy Mater Sol. Cells* **2007**, *91*, 986-995.

(4) Nishida, K.; Ohnishi, A.; Kitaura, M.; Sasaki, M.; Kuriyama, Y., Optical Absorption of Cdi2single Molecule and Clusters Incorporated into Zeolite Na-Fau. *J. Phys. Soc. Japan* **2009**, *78*.

(5) Xu, D.; Wang, S. Y.; Wu, B. S.; Zhang, B.; Qin, Y.; Huo, C. F.; Huang, L. H.; Wen, X. D.; Yang, Y.; Li, Y. W., Highly Dispersed Single-Atom Pt and Pt Clusters in the Fe-Modified Kl

Zeolite with Enhanced Selectivity for N-Heptane Aromatization. *Acs. Appl. Mater. Inter.* **2019**, *11*, 29858-29867.

(6) Sun, Q. M.; Wang, N.; Zhang, T. J.; Bai, R.; Mayoral, A.; Zhang, P.; Zhang, Q. H.; Terasaki, O.; Yu, J. H., Zeolite-Encaged Single-Atom Rhodium Catalysts: Highly-Efficient Hydrogen Generation and Shape-Selective Tandem Hydrogenation of Nitroarenes. *Angew. Chem. Int. Ed.* **2019**, *58*, 18570-18576.

(7) Qiu, J. Z.; Hu, J. B.; Lan, J. G.; Wang, L. F.; Fu, G. Y.; Xiao, R. J.; Ge, B. H.; Jiang, J. X., Pure Siliceous Zeolite-Supported Ru Single-Atom Active Sites for Ammonia Synthesis. *Chem. Mater.* **2019**, *31*, 9413-9421.

(8) Dong, B.; Retoux, R.; de Waele, V.; Chiodo, S. G.; Mineva, T.; Cardin, J.; Mintova, S., Sodalite Cages of Emt Zeolite Confined Neutral Molecular-Like Silver Clusters. *Micropor. Mesopor. Mat.* **2017**, *244*, 74-82.

(9) Nozue, Y.; Tang, Z. K.; Goto, T., Excitons in Pbi2 Clusters Incorporated into Zeolite Cages. *Solid State Commun.* **1990**, *73*, 531-534.

(10) Tang, Z. K.; Nozue, Y.; Goto, T., Quantum Size Effect on the Excited-State of Hgi2, Pbi2 and Bii3 Clusters and Molecules in Zeolite Lta. *J. Phys. Soc. Japan* **1992**, *61*, 2943-2950.

(11) Tang, Z. K.; Nozue, Y.; Terasaki, O.; Goto, T., Frenkel Excitons in Ordered Pbi2 Clusters Incorporated into Zeolite. *Molecular Crystals and Liquid Crystals Science and Technology. Section A. Mol. Cryst. Liq.* **2006**, *218*, 61-66.

(12) Sarwar, S.; Ko, K.-W.; Han, J.; Han, C.-H.; Jun, Y.; Hong, S., Improved Long-Term Stability of Dye-Sensitized Solar Cell by Zeolite Additive in Electrolyte. *Electrochim. Acta* **2017**, *245*, 526530.

(13) Lee, H.; Kim, H. S., Work-Function Engineering in Lead Sulfide and Cadmium Sulfide Quantum Dots Incorporated into Zeolite Y Using Ion Exchange. *Part. Part. Syst. Charact.* **2016**, *33*, 126-131.

(14) Baekelant, W., et al., Confinement of Highly Luminescent Lead Clusters in Zeolite A. *J. Phys. Chem. C* **2018**, *122*, 13953139 61.

(15) Leiggener, C.; Calzaferri, G., Synthesis and Luminescence Properties of Ag2s and Pbs Clusters in Zeolite A. *Chem. Eur. J.* **2005**, *11*, 7191-7198.

(16) Fenwick, O., et al., Tuning the Energetics and Tailoring the Optical Properties of Silver Clusters Confined in Zeolites. *Nat. Mater.* **2016**, *15*, 1017-22.

(17) Terasaki, O.; Tang, Z. K.; Nozue, Y.; Goto, T., Pbi2 Confined in the Spaces of Lta Zeolites. *Mater. Res. Soc. Symp. P* **1991**, *233*, 139-143.

(18) De Cremer, G., et al., Characterization of Fluorescence in Heat-Treated Silver-Exchanged Zeolites. *J. Am. Chem. Soc.* **2009**, *131*, 3049-56.

(19) http://www.iza-online.org Http://Www.Iza-Online.Org.

(20) Ming, D.; Allen, E., Use of Natural Zeolites in Agronomy, Horticulture, and Environmental Soil Remediation. *Rev. Mineral. Geochem.* **2001**, *45*, 619-654.

(21) Moliner, M.; Diaz-Cabanas, M. J.; Fornes, V.; Martinez, C.; Corma, A.; , Synthesis Methodology, Stability, Acidity, and Catalytic Behavior of the 18 X 10 Member Ring Pores Itq-33 Zeolite. *J. Catal.* **2008**, *254*, 101–109.

(22) Kokotailo, G. T.; Ciric, J., Synthesis and Structural Features of Zeolite Zsm-3. *Adv. Chem. Ser.* **1971**, *101*, 109-121.

(23) Delprato, F.; Delmotte, L.; Guth, J. L.; Huve, L., Synthesis of New Silica-Rich Cubic and Hexagonal Faujasites Using Crown-Ether-Based Supramolecules as Templates. *Zeolites* **1990**, *10*, 546-552.

(24) Baerlocher, C.; McCusker, L. B.; Chiappetta, R., Location of the 18-Crown-6 Template in Emc-2 (Emt). Rietveld Refinement of the Calcined and as-Synthesized Forms. *Micropor. Mesopor. Mat.* **1994**, *2*, 269-280.

(25) Derakhshankhah, H.; Jafari, S.; Sarvari, S.; Barzegari, E.; Moakedi, F.; Ghorbani, M.; Varnamkhasti, B. S.; Jaymand, M.; Izadi, Z.; Tayebi, L., Biomedical Applications of Zeolitic Nanoparticles, with an Emphasis on Medical Interventions. *Int. J. Nanomed.* **2020**, *15*, 363-386.

(26) Chen, X. Y.; Nik, O. G.; Rodrigue, D.; Kaliaguine, S., Mixed Matrix Membranes of Aminosilanes Grafted Fau/Emt Zeolite and Cross-Linked Polyimide for CO2/CH4 Separation. *Polymer* **2012**, *53*, 3269-3280.

(27) Kim, S. H.; Lim, W. T.; Kim, G. H.; Lee, H. S.; Heo, N. H., Synthesis and Crystal Structure of Lead Iodide in the Sodalite Cavities of Zeolite a (Lta). *B. Kor. Chem. Soc.* **2006**, *27*, 679-686.

(28) Kim, H. S.; Yoon, K. B., Preparation and Characterization of Cds and Pbs Quantum Dots in Zeolite Y and Their Applications for Nonlinear Optical Materials and Solar Cell. *Coord. Chem. Rev.* **2014**, *263-264*, 239-256.

(29) Chen, W.; Wang, Z. G.; Lin, Z. J.; Qian, J. J.; Lin, L. Y., New Observation on the Formation of Pbs Clusters in Zeolite-Y. *Appl. Phys. Lett.* **1996**, *68*, 1990-1992.

(30) Kim, S. H.; Heo, N. H.; Kim, G. H.; Hong, S. B.; Seff, K., Preparation, Crystal Structure, and Thermal Stability of the Cadmium Sulfide Nanoclusters Cd6s44+ and Cd2na2s4+in the Sodalite Cavities of Zeolite a (Lta). *J. Phys. Chem. B* **2006**, *110*, 2596474.

(31) Togashi, N.; Sakamoto, Y.; Ohsuna, T.; Terasaki, O., Arrayed Pbi2 Clusters in the Spaces of Zeolite Lta. *Mat. Sci. Eng. aStruct.* **2001**, *312*, 267-273.

(32) Ye, S.; Sun, J. Y.; Han, Y. H.; Zhou, Y. Y.; Zhang, Q. Y., Confining Mn(2+)-Doped Lead Halide Perovskite in Zeolite-Y as Ultrastable Orange-Red Phosphor Composites for White LightEmitting Diodes. *ACS Appl. Mater. Interfaces* **2018**, *10*, 24656 24664.

(33) Li, C.; Zhang, Q.; Mayoral, A., Ten Years of Aberration Corrected Electron Microscopy for Ordered Nanoporous Materials. *ChemCatChem* **2020**, *12*, 1248-1269.

(34) Mayoral, A.; Angel, P. d.; Ramos, M., Electron Microscopy Techniques to Study Structure/Function Relationships in Catalytic Materials. In *Advanced Catalytic Materials: Current Status and Future Progress*, Domínguez-Esquivel, J.; Ramos, M. M., Eds. Springer, Cham: 2019; pp 97-128.

(35) Li, J.; Zhang, C.; Jiang, J.; Yu, J.; Terasaki, O.; Mayoral, A., Structure Solution and Defect Analysis of an Extra-Large Pore Zeolite with Utl Topology by Electron Microscopy. *J. Phys. Chem. Lett.* **2020**, *11*, 3350-3356.

(36) Mayoral, A., et al., Direct Atomic-Level Imaging of Zeolites: Oxygen, Sodium in Na-Lta and Iron in Fe-Mfi. *Angew. Chem. Int. Ed.* **2020**, *59*, 19361-19721.

(37) Zhang, Q.; Mayoral, A.; Li, J.; Ruan, J.; Alfredsson, V.; Ma, Y.; Yu, J.; Terasaki, O., Electron Microscopy Studies of Local Structural Modulations in Zeolite Crystals. *Angew. Chem. Int. Ed.* **2020**, 19403-19413.

(38) Okunishi, E.; Ishikawa, I.; Sawada, H.; Hosokawa, F.; Hori, M.; Kondo, Y., Visualization of Light Elements at Ultrahigh Resolution by Stem Annular Bright Field Microscopy *Microsc. Microanal.* **2009**, *15*, 164-165.

(39) Okunishi, E.; Sawada, H.; Kondo, Y., Experimental Study of Annular Bright Field (Abf) Imaging Using AberrationCorrected Scanning Transmission Electron Microscopy (Stem). *Micron* **2012**, *43*, 538–544.

(40) Weitkamp, J.; Schumacher, R. Proceed. Ninth hit. Zeo. Conf., Ballmoos, R. v.; Higgins, J. B.; Treacy, M. M. J., Eds. Butterworth-Heinemann: 1993; p 353.

(41) Burla, M. C.; Caliandro, R.; Carrozzini, B.; Cascarano, G. L.; Cuocci, C.; Giacovazzo, C.; Mallamo, M.; Mazzone, A.; Polidori, G., Crystal Structure Determination and Refinement Via Sir2014. *J. Appl. Cryst.* **2015**, *48*, 306–309.

(42) Woo, J.; Guliants, V. V., Qstem-Based Haadf-Stem Image Analysis of Mo/V Distribution in Movtetao M1 Phase and Their Correlations with Surface Reactivity. *Appl. Catal. a-Gen.* **2016**, *512*, 27-35.

(43) Ishizuka, K.; Eilers, P. H. C.; Kogure, T., Optimal Noise Filters in High-Resolution Electron Microscopy *Micros. Today* **2007**, 16-20.

(44) Terasaki, O.; Ohsuna, T., What Can We Observe in Zeolite Related Materials by Hrtem? *Catal. Today* **1995**, *23*, 201-218.

(45) Alfredsson, V.; Ohsuna, T.; Terasaki, O.; Bovin, J. O., Investigation of the Surface Structure of the Zeolites Fau and Emt by High-Resolution Transmission Electron Microscopy. *Angew. Chem. Int. Ed.* **1993**, *32*, 1210-1213.

(46) Anderson, M. W.; Pachis, K. S.; Prebin, F.; Carr, S. W.; Terasaki, O.; Ohsuna, T.; Alfreddson, V., Intergrowths of Cubic and Hexagonal Polytypes of Faujasitic Zeolites. *J. Chem. Soc. Chem. Comm.* **1991**, 1660-1664.

(47) Treacy, M. M. J.; Vaughan, D. E. W.; Strohmaier, K. G.; Newsam, J. M., Intergrowth Segregation in Fau-Emt Zeolite Materials. *P Roy Soc a-Math Phy* **1996**, *452*, 813-840.

(48) González, G.; González, C. S.; Stracke, W.; Reichelt, R.; García, L., New Zeolite Topologies Based on Intergrowths of Fau/Emt Systems. *Micropor. Mesopor. Mat.* **2007**, *101*, 30-42.

(49) Okunishi, E.; Ishikawa, I.; Sawada, H.; Hosokawa, F.; Hori, M.; Kondo, Y., Visualization of Light Elements at Ultrahigh Resolution by Stem Annular Bright Field Microscopy. *Microsc. Microanal.* **2009**, *15*, 164-165.

(50) Findlay, S. D.; Shibata, N.; Sawada, H.; Okunishi, E.; Kondo, Y.; Ikuhara, Y., Dynamics of Annular Bright Field Imaging in Scanning Transmission Electron Microscopy. *Ultramicroscopy* **2010**, *110*, 903-923.

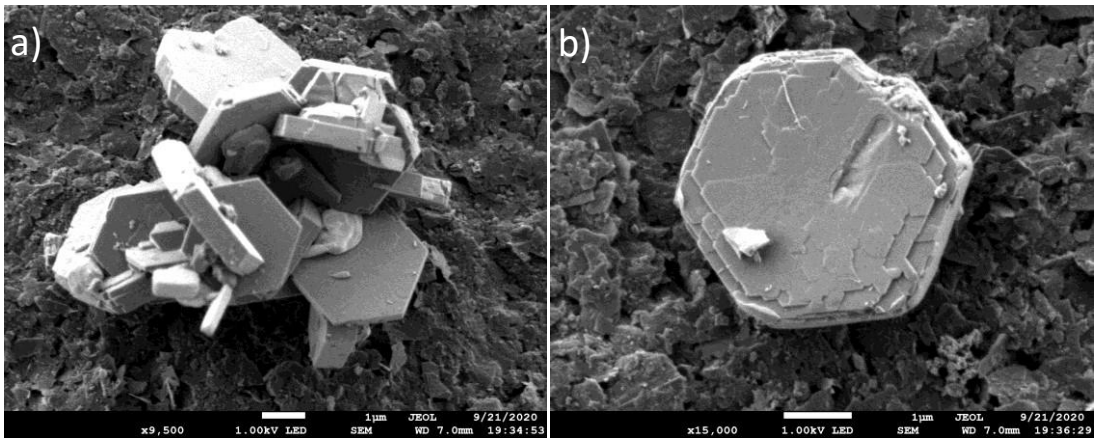

Figure 1. a) Low magnification SEM image of several **EMT** particles. b) SEM image of an isolated **EMT** crystal with hexagonal plate morphology.

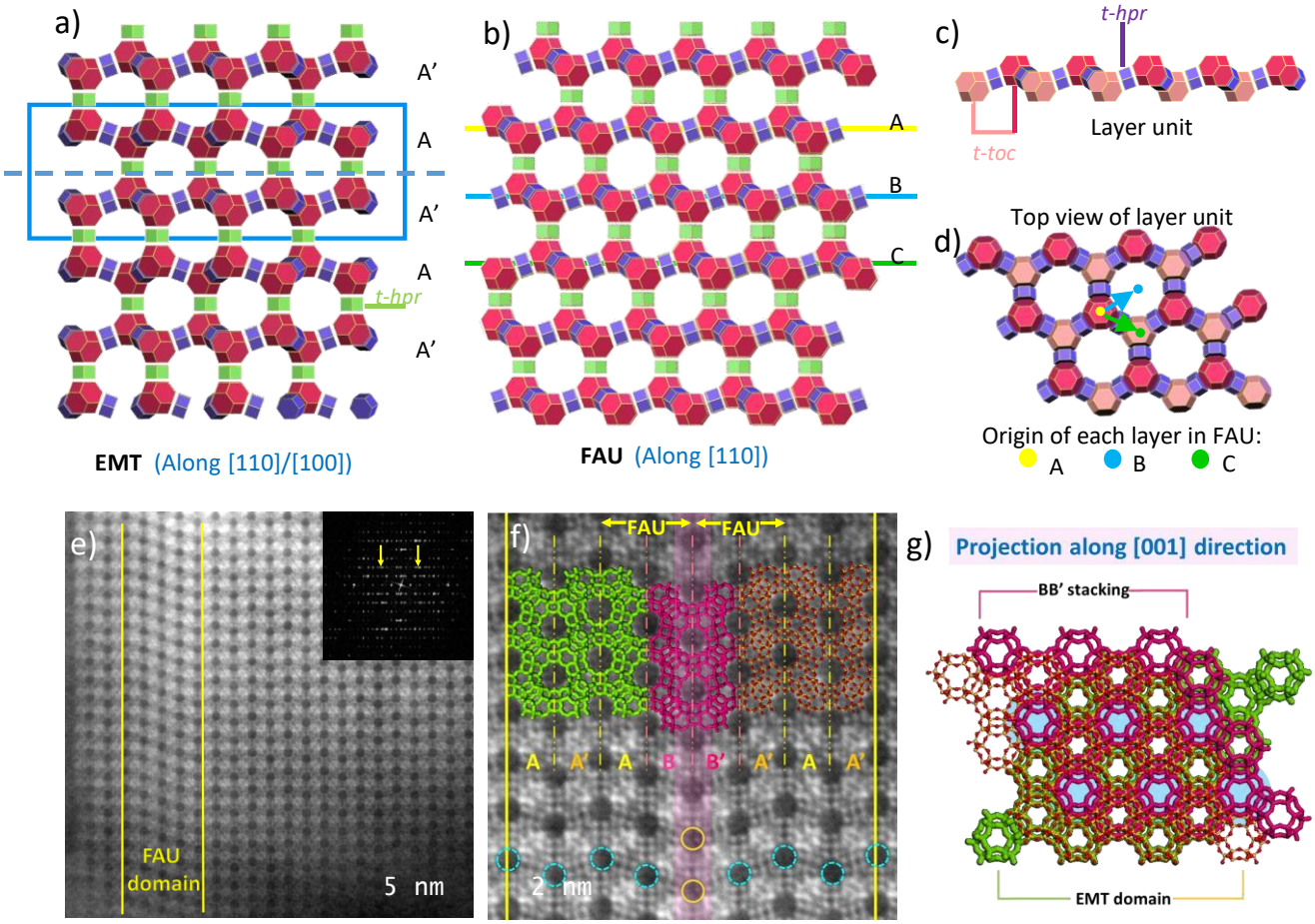

Figure 2. a) **EMT** model along $[110]/[100]_{EMT}$ orientation. b) **FAU** model along [110]. c) Schematic model of a layer unit (*faujasite* layer), front view. d) Top view of the model corresponding to a layer unit. The origins for the subsequent layers are marked by yellow, blue and green dots. Color code: Rose cages correspond to *t-toc* (sodalite cages); *t-hpr* (double 6-membered ring, D6R) appear in green (between layers) and in purple (within per layer) cages. e) C_s-corrected STEM-ADF micrograph recorded along the $[110]/[100]_{EMT}$ with a **FAU** intergrowth marked by yellow lines. The Fourier Diffractogram (FD) is shown inset with yellow arrows pointing at the diffuse streaks. f) Closer observation of another crystal where two **FAU** domains are joint by a mirror plane BB'. The dashed blue circles correspond to the 12MRs, while the yellow ones denote the partial blocked 12MRs within the twin plane. g) Schematic representation of the structure model of f) along $[001]_{EMT}$ direction.

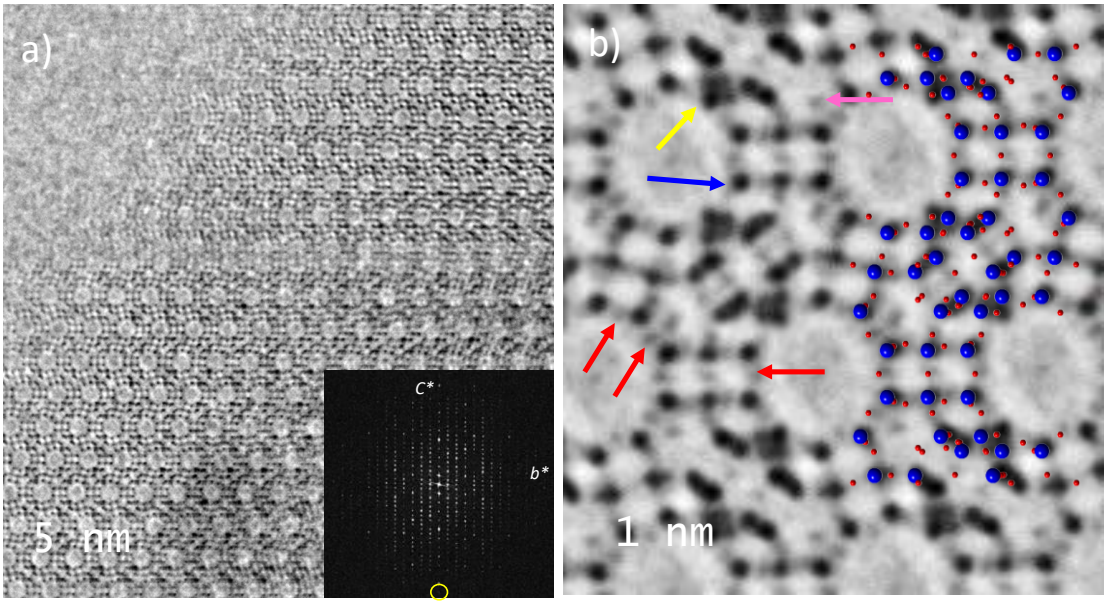

Figure 3. C_s-corrected STEM-ABF data of Pb-**EMT**. a) Atomic resolution data along [100] projection with the FD shown inset. The white arrow corresponds to a structural defect. The yellow circle in the FD indicates the maximum transfer information corresponding to the 00024 spot. b) Symmetry *pmg* averaged data with the framework model superimposed. The red arrows point at O bridges, the blue one corresponds to the T atoms, and the yellow and pink ones to extraframework signals.

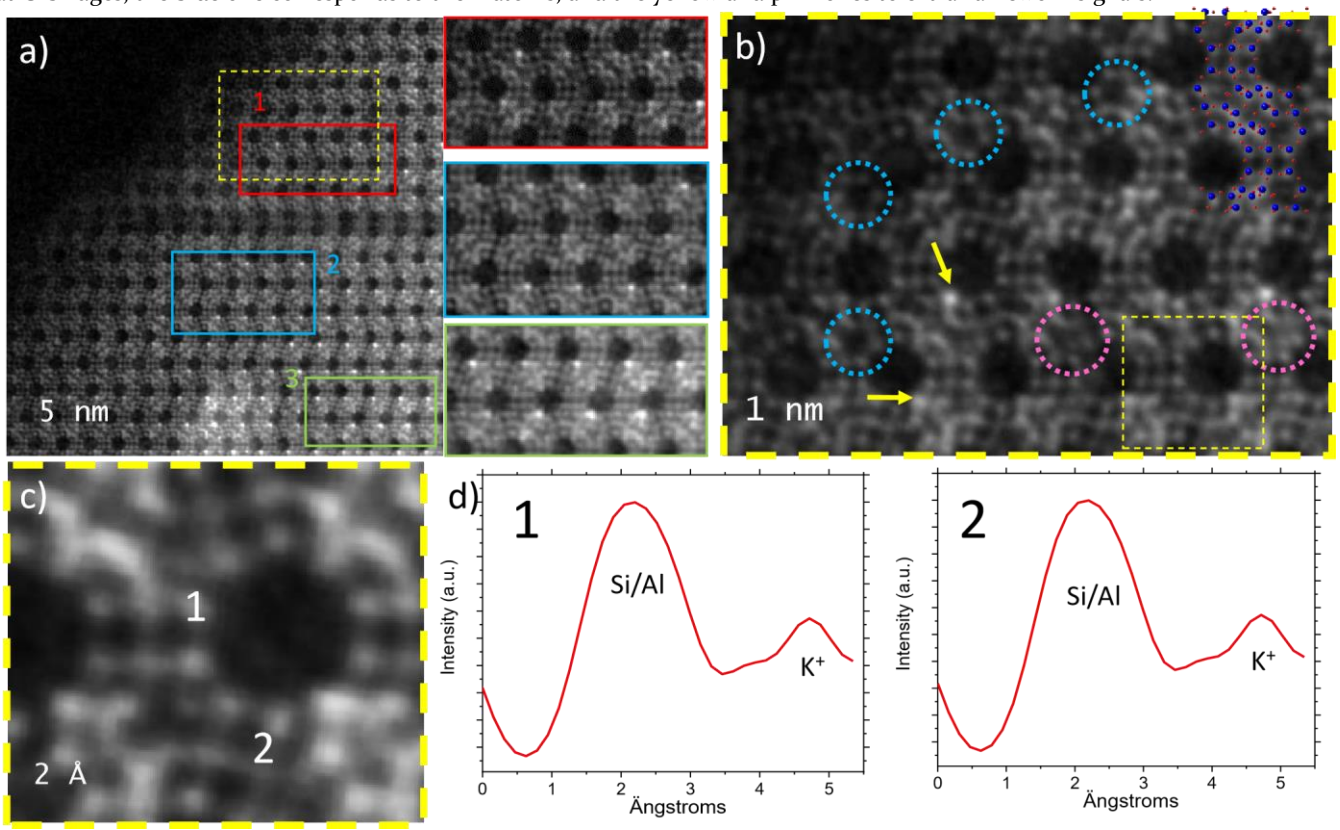

Figure 4. a) C_s-corrected STEM-ADF along [100] of Pb-**EMT**. The three colored rectangles correspond to the areas where the intensity analysis was performed. The dashed yellow rectangle indicates where figure b) was obtained from. b) Closer observation of the framework where the bright sports are marked by yellow arrows. An empty s6R is denoted by a dashed blue circle. The dashed pink circle corresponds to a s6R with a cation inside. c) Enlarged image of a s6R where the two arrows indicate where the intensity profiles where extracted from, numbered as 1 and 2. d) Intensity profiles along 1 and 2.

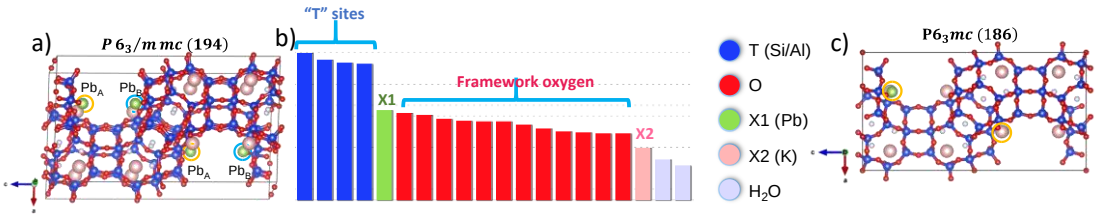

Figure 5. a) Structural solution using *P*6$_3$/*mmc* (194). b) Intensity histogram from the 3D-EDT diffraction reflections with space group P6$_3$/*mmc*. c) Structural model after removing Pb$_A$ or Pb$_B$ leading into a lower symmetry *P*6$_3$*mc*.

TOC Graphic